Estimating Ionospheric Height From Amplitude Scintillation Signatures in SAR Images

Felipe Betancourt-Payan, *Graduate Student Member, IEEE*, Jun Su Kim, *Member, IEEE*, Konstantinos P. Papathanassiou, *Fellow, IEEE*, Marc Rodriguez-Cassola, and Gerhard Krieger, *Fellow, IEEE*

***Abstract*— In this letter, we discuss the estimation of the location of ionospheric irregularities exploiting the appearance of intensity scintillations in ALOS-2 images, as they are semifocused at different heights. The intensity scintillations (stripes) are not always visible in the single-look complex (SLC) images. However, they start to be visible, as the image is semifocused at different heights with a peak of contrast where electron density irregularities are found (ionospheric height). The slant range between the satellite and the ionospheric plane can be estimated and converted directly into the ionospheric height by autofocusing the stripes. The observations show good agreement with the height of maximum ionization estimated by the International Reference Ionosphere (IRI). Furthermore, we perform an alternative geometric validation based on feature tracking by comparing the shifts between azimuth sublooks. With both methods for the presented dataset, the height of the ionospheric irregularities was estimated to be 330 km.**

***Index Terms*— Intensity scintillation, ionosphere, synthetic aperture radar (SAR).**

I. Introduction

LOW-FREQUENCY synthetic aperture radar (SAR) images are affected by the two-way passage of the radar waves through the ionosphere in different ways (phase errors, delays, Faraday rotation, and scintillation) [1], [2]. All these effects are related to the total electron content (TEC) and its spatial variation. The TEC has a background component that changes slowly and a turbulent component made of electron density irregularities with outer scales as small as a few kilometers [3], [4], [5]. These irregularities are mostly found within the F2 layer of the ionosphere, the region of maximum ionization that extends approximately between 200 and 400 km. Ionospheric irregularities form in a narrow region within this layer that, in practice, will be approximated to a thin layer at the so-called ionospheric height h_{iono} [6], [7], [8]. It should be emphasized that this height is not necessarily the height of maximum background ionization.

Turbulent irregularities are typical in equatorial and polar latitudes [9]. Around the equator, the irregularities are elongated blobs or bubbles [10] that can produce scintillation. Scintillations are rapid phase variations added to the SAR data that, when not compensated, produce defocusing [2]. The diffraction experienced by the radar waves as they exit the irregular phase modulation inside the ionosphere and further propagate in nearly free space [7], [11], [12], [13] can also produce intensity scintillation patterns. These are commonly seen as elongated intensity stripes aligned to the geomagnetic field direction as found in ALOS images in equatorial regions [14], [15], [16].

The intensity scintillation will not always be visible in the focused images if the geomagnetic field is not aligned with the azimuth direction. The reason for this is that the ionosphere is between the satellite and the ground, so the stripe pattern is smeared by the processing of the synthetic aperture [17]. This letter proposes a method to estimate the height at which the ionospheric irregularities are located directly from the data based on the observation of amplitude scintillation when semifocusing the image at different heights [18]. By semifocusing, the azimuth matched filter parameters are adapted to gain resolution at different slant ranges (other than the one from the satellite to the targets on ground) and autofocus the ionospheric features. The slant range from the satellite to the ionosphere and the ionospheric height can be extracted from the derived azimuth matched filter.

The ionospheric height estimation by semifocusing is compared with the one obtained by exploring feature tracking in azimuth sublooks. When separating one sub-band of the azimuth spectrum, it is as if a smaller synthetic aperture was processed. Then, one loses resolution in the image on the ground, but it enables detection and tracking of amplitude scintillations. With a geometric inversion, one can also estimate the ionospheric height.

Estimates of the height of maximum ionization can be obtained from models, such as NeQuick [19] and International Reference Ionosphere (IRI) [20], based on the electron density profiles. The models focus on the background component of the ionosphere, and the height of maximum ionization is not exactly the height where irregularities are found. In addition, to circumvent the model limitations, it is preferred to estimate the location of the irregularities directly from the data. In the polar regions, where good Faraday rotation sensitivity is given, it is possible to estimate the ionospheric height from the fully polarimetric data using a parallax between the Faraday rotation azimuth sublooks [18]. The Faraday rotation parallax does not work well closer to the equator, where the Faraday rotation

Manuscript received 19 March 2024; revised 24 June 2024; accepted 16 July 2024. Date of publication 19 July 2024; date of current version 31 July 2024. This work was supported by German Academic Exchange Service (DAAD) under Grant 57478193. *(Corresponding author: Felipe Betancourt-Payan.)*

The authors are with the Microwaves and Radar Institute, German Aerospace Center (DLR), 82234 Weßling, Germany (e-mail: felipe.betancourtpayan@dlr.de).

Digital Object Identifier 10.1109/LGRS.2024.3431023

sensitivity is low. On the other hand, the method proposed in this letter uses the intensity scintillation signature in single images and is polarization-independent. Because of the high anisotropic nature of equatorial irregularities, this method is meant to be exploited in low latitudes.

Section II describes the observations and method used to process the data. In Section III, the height inversion method is shown to validate the observations geometrically. Finally, Section IV summarizes the findings.

II. Amplitude Scintillation in Semifocused Images

Fig. 1 shows a simplified version of the SAR observation geometry, including the ionosphere. The platform moves along the x-axis and the y-axis points in the slant range direction, with the slant range to a given range bin R_0. The platform flies at the height of h_{sat}. The plane where the irregularities form (ionospheric plane) is located between the satellite and the ground at a height h_{iono}, and the slant ranges to the satellite and ground are R_{iono} and R'_{iono}, respectively. Even if a flat Earth and rectilinear motion geometry are shown in Fig. 1, the Earth's ellipsoid and exact orbit available in the dataset are considered in the following. However, it is always straightforward to relate h_{iono} to R_{iono} or R'_{iono}.

Semifocusing SAR images at h_{iono} is a well-known practice to inject and correct for ionospheric effects, such as phase advance and Faraday rotation [8], [18], of the turbulent ionosphere. By doing so, the resolution at which the ionospheric disturbances are visible is only limited by the azimuth and range bandwidths. Semifocusing can be done by modifying the slant range either to the ground or to the ionospheric plane from the satellite orbit, R, and the corresponding effective velocity, v, in the azimuth matched filter

$$H_{\text{ac}}(f_a, R) = \exp\left[j \cdot \frac{4 \cdot \pi \cdot R}{\lambda}(\zeta(f_a) - 1)\right] \tag{1}$$

with

$$\zeta(f_a) = \sqrt{1 - \left(\frac{f_a \cdot \lambda}{2 \cdot v}\right)^2}$$

where f_a is the azimuth frequency and λ is carrier wavelength. A detailed explanation can be found in [18].

Starting from the range compressed data, when compressing at any height other than h_{iono}, the contribution of ionospheric resolution cell spreads into the neighboring image resolution cells. Consequently, if the image is focused on the ground, the ionospheric signatures of phase delay, Faraday rotation, and amplitude scintillation are smeared by an averaging along azimuth. The size of the averaging window is the one of the synthetic apertures projected on the ionospheric plane. The smearing becomes less apparent for highly anisotropic irregularities aligned to the azimuth direction [21].

Fig. 2 summarizes the processing steps. Our starting point is the full-polarimetric set of single-look complex (SLC) images of ALOS-2 (ALOS2050060000) without apparent amplitude modulation, together with the orbit and scene coordinates. We also choose an initial value for the irregularity height, which is used to calculate the slant range between the satellite orbit and the ionospheric coordinates. The parameters of the

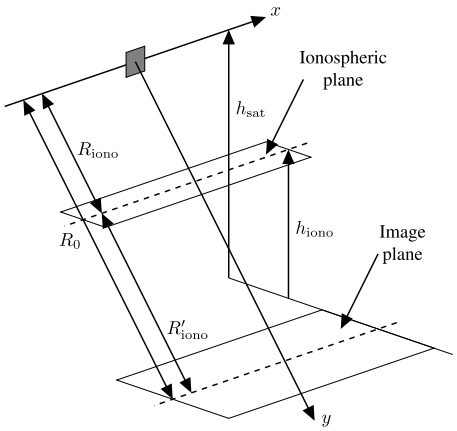

Fig. 1. Simplified SAR observation geometry.

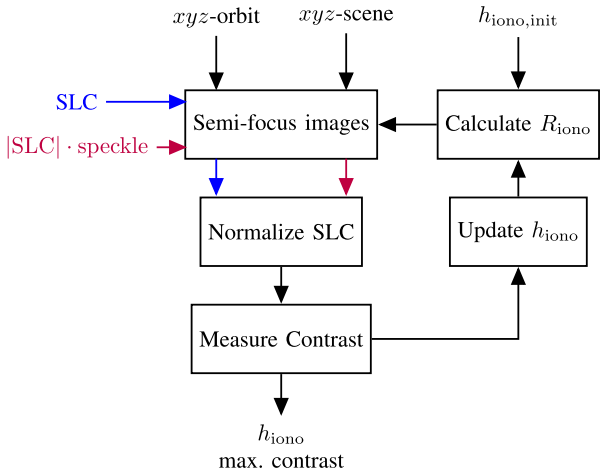

Fig. 2. Algorithm block diagram.

dataset used in our investigation are summarized in Table I. Fig. 3 shows the SLC of the HV channel (amplitude scintillation is better seen in the cross-pol channels of the current dataset, but they are indeed present in all other channels too). As the SLC images are semifocused at different ionospheric heights, stripe-like patterns start to appear, as shown in Fig. 4. Note that the stripes follow the geomagnetic field projected on the image plane (white line), which is off the azimuth direction, and the ionospheric signature appears superimposed on the azimuth defocusing of the scene.

For a better characterization of the stripes, it is necessary to normalize and remove the background scene component. A logical way to obtain semifocused images without the background component is to normalize with the amplitude of a semifocused image without phase modulation introduced by the ionosphere. This was obtained by taking the amplitude of the SLC images and adding multiplicative complex speckle. Hence, the phase modulation goes away, but the amplitude image bandwidth expands and can be decompressed with the matched filter. Fig. 5 shows the normalized HV images semifocused at different ionospheric heights. Note the different levels of contrast or sharpness of the stripes.

As shown in Fig. 6, an iterative autofocus approach can be used to update the h_{iono} value and estimate the R_{iono} for which the intensity stripes have maximum contrast and invert

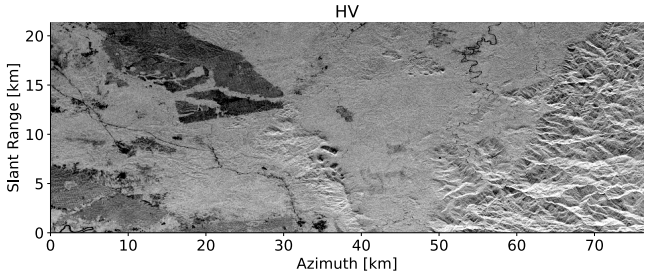

Fig. 3. SLC intensity of the HV channel of an ALOS-2 image. The forest scene is located in Indonesia, very close to the geomagnetic equator.

TABLE I
OBSERVATION PARAMETERS OF THE ALOS2050060000 DATASET

Parameter	Unit	Value
Coordinates center image (lon, lat)	(deg, deg)	(116, 0.63)
Date	YYYY/MM/DD	2015/04/27
Time	hh:mm:ss	16:26:33
Pulse repetition frequency (PRF)	Hz	2320.8627
Incidence angle (θ_{inc})	deg	31.086
Azimuth oversampling (aosf)	-	0.3888
Satellite height (h_{sat})	km	634.285
Range to ground (R_0)	km	728.84
Doppler rate (K_{t})	Hz/s	-607.08432
Central frequency (f_0)	GHz	1.2575

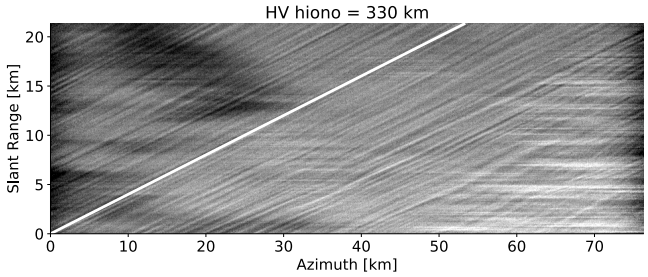

Fig. 4. Non-normalized SLC image semifocused images at 330 km. The white line shows the geomagnetic field projected on the image planes.

for h_{iono}. The best-performing contrast metric for this task was the variance of the gray level [22]. In this case, an ionospheric height of 330 km is estimated with the current method and is compared with the height of maximum ionization in the F2 layer (hmF2) according to the IRI model. Note that models like the IRI present drawbacks, such as limited precision, coarse resolution, and only focus on the background ionosphere. However, due to the high resolution of SAR, we are sensitive to lower scale variations, and even under the thin layer approximation, instead of the height of maximum ionization, we are interested in the height that better represents the location of the irregularities. For this reason, even though the models are a good starting point in practice, it is essential to rely on direct estimations.

III. GEOMETRIC VALIDATION

The ionospheric height estimation can be validated geometrically using azimuth sublooks. The principle is based on the fact that anything at a height different from the (semi-)focused image will appear to shift from the beam center while taking azimuth sub-bands. It is possible to look at it

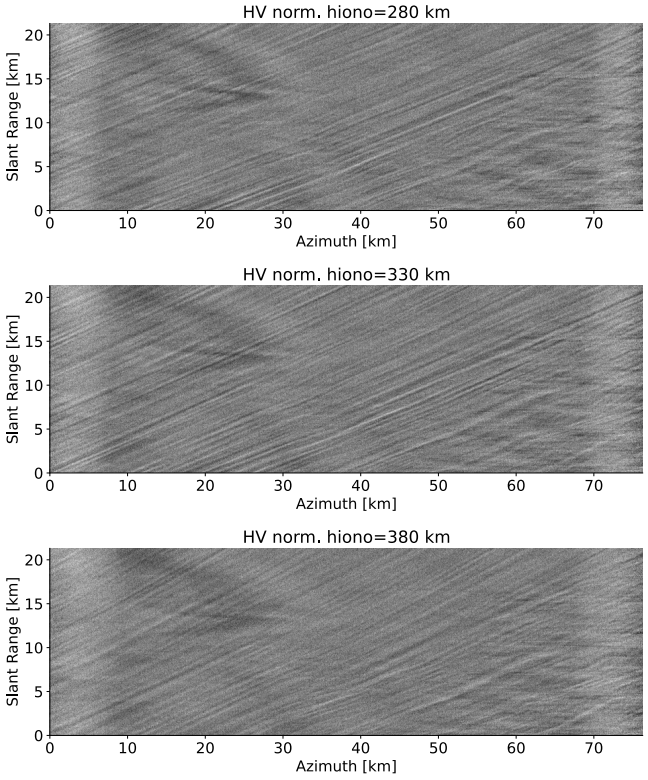

Fig. 5. Normalized SLC semifocused at different ionospheric heights: 280 km (top), 330 km (middle), and 380 km (bottom).

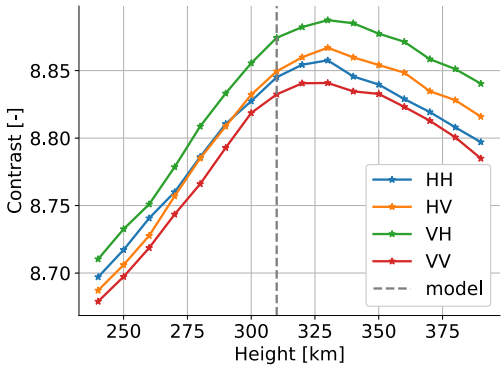

Fig. 6. Stripe contrast change with ionospheric height. As a reference, the height of maximum ionization of the F2 layer, as taken from the IRI model, is indicated by a vertical dashed line.

like this: when the image is fully focused (on ground), the ionosphere is defocused in azimuth by a quadratic phase error

$$\phi_\epsilon\left(R'_{\text{iono}}; f_a\right) = \frac{4 \cdot \pi \cdot R'_{\text{iono}}}{\lambda} \cdot \zeta\left(f_a\right) \tag{2}$$

and R'_{iono} can be inverted from azimuth-sublook cross correlation, similar to what would be done in a map-drift autofocus [23]. Here, the quadratic error across the whole image is constant, and many sublooks are taken instead of operating by blocks.

We start from the SLC images and take 32 nonoverlapping azimuth sublooks (the added sublook bandwidths extend to the image azimuth bandwidth). As an example, the amplitude of one of the sublooks is shown in Fig. 7, which has been normalized with the mean amplitude value of all other sublooks to remove the background scene component. Here, the amplitude

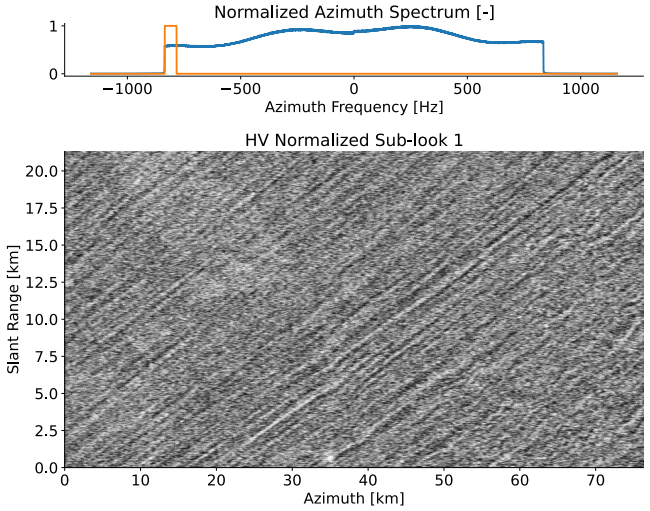

Fig. 7. Stripe pattern in an amplitude image of a normalized sublook, 1/32th of azimuth bandwidth.

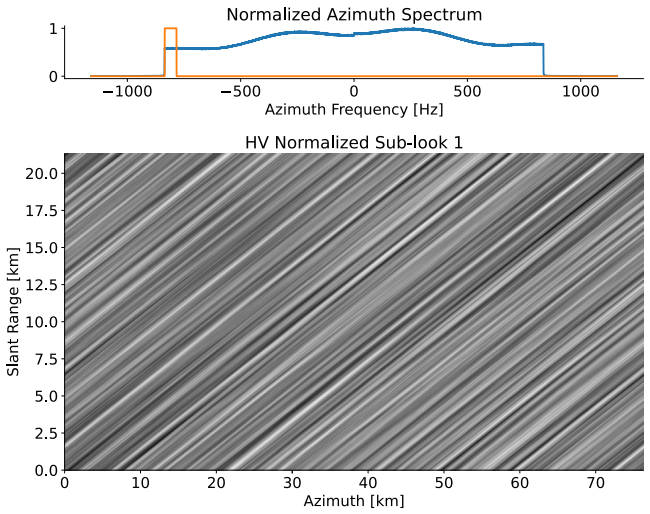

Fig. 8. Normalized sublook after a 10-pixel directional averaging along the geomagnetic field line.

stripes clearly appear, because, at the expense of lowering the resolution of the SLC image, the resolution of the ionosphere irregularities is increased by the shorter processed synthetic aperture [17]. By taking different sublooks, the feature drifts along azimuth and by tracking it, it is possible to invert for R'_{iono} and again for h_{iono}. Another method to take into consideration for the separation of the stripe pattern is the bandpass filtering in the direction of the geomagnetic field, as described in [24].

It was necessary to preprocess the data with an averaging filter oriented in the geomagnetic field to improve the accuracy in estimating along the drift between normalized sublooks. See the averaged data in Fig. 8.

It is known that due to the azimuth frequency to squint-angle relation [25], one can relate any azimuth frequency, f_a, to a corresponding squint angle off the zero Doppler, β_a

$$\sin(\beta_a) = \frac{\lambda \cdot f_a}{2 \cdot v}. \tag{3}$$

With R'_{iono} being the slant range from the ground to the ionospheric plane, the drift of the ionospheric pattern between

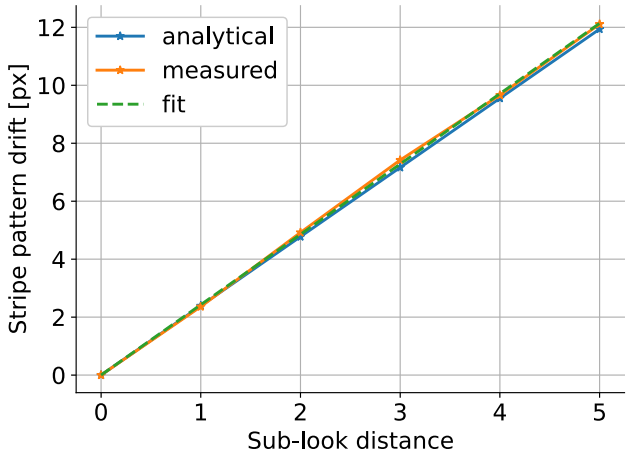

Fig. 9. Scintillation pattern drift estimated from azimuth sublooks that are separated by up to five consecutive nonoverlapping sublooks.

two consecutive sublooks with center frequencies $f_{a,1}$ and $f_{a,2}$ can be approximated to

$$\Delta x = R'_{\text{iono}} \cdot \left(\tan\left(\beta_{a,2}\right) - \tan\left(\beta_{a,1}\right)\right) \tag{4}$$

in meters. This can be translated into pixels, Δpx, as follows:

$$\Delta\text{px} = \frac{\Delta x}{v} \cdot \Delta f. \tag{5}$$

with

$$\Delta f = \frac{\text{PRF}}{N_{\text{sl}} \cdot (1 + \text{aosf})} \tag{6}$$

and aosf the azimuth oversampling factor.

Fig. 9 shows the drift of the amplitude scintillation pattern along azimuth for sublooks separated by up to five consecutive sublooks, measured by cross correlation (no drift in range was observed). In blue, there is the expected drift as given by (5), and the measurements are in orange. Including Earth's ellipsoid, for an h_{iono} of 330 km, R'_{iono} is 381.895 km, the pixel distance between consecutive sublooks is 2.42, and the slope of the fit in green is 2.38. Note the good agreement in the slope, which points out that the altitude estimation and R'_{iono} are very similar.

IV. Conclusion

This letter presents an autofocus method for estimating the height of ionospheric irregularities at equatorial latitudes based on the analysis of intensity scintillations. The methodology is tested with an ALOS-2 dataset. In this dataset, where the geomagnetic field does not align with the trajectory, the intensity scintillations smear with the synthetic aperture and are not visible in the focused image. The ionospheric irregularities start to become visible when semifocusing the image at different heights, and the contrast is maximum at the height where the irregularities are found (assumed they extend over a narrow enough region to be approximated to a thin layer), because their resolution is maximum too. This allows the estimation of the ionospheric height directly from the data based on contrast metrics. A geometric validation was made using feature tracking in azimuth sublooks. When taking nonoverlapping azimuth sublooks and normalizing to remove the background, it is possible to see that the irregularity

features drift along azimuth. By measuring the drift, it is also possible to estimate the ionospheric height, further confirming the reliability and accuracy of our method.

It is imperative to know the ionospheric height precisely to calibrate SAR images correctly. The benefits of the methods proposed in this letter are that they do not rely on models (as shown in Section II) and that they have shown to work well even at equatorial latitude (where Faraday rotation-based methods, such as the ionospheric parallax, have low sensitivity) with single images.

REFERENCES

[1] Z.-W. Xu, J. Wu, and Z.-S. Wu, "A survey of ionospheric effects on space-based radar," *Waves Random Media*, vol. 14, no. 2, pp. S189–S273, Apr. 2004.

[2] D. P. Belcher, "Theoretical limits on SAR imposed by the ionosphere," *IET Radar, Sonar Navigat.*, vol. 2, no. 6, pp. 435–448, Dec. 2008.

[3] Y.-H. Liu, C.-H. Liu, and S.-Y. Su, "Global and seasonal scintillation morphology in the equatorial region derived from ROCSAT-1 in-situ data," *Terr., Atmos. Ocean. Sci.*, vol. 23, no. 1, pp. 95–106, 2012.

[4] S. Basu, S. Basu, and B. K. Khan, "Model of equatorial scintillations from in-situ measurements," *Radio Sci.*, vol. 11, no. 10, pp. 821–832, Oct. 1976.

[5] K. C. Yeh and C. H. Liu, "Diagnosis of the turbulent state of ionospheric plasma by propagation methods," *Radio Sci.*, vol. 12, no. 6, pp. 1031–1034, Nov. 1977.

[6] C. L. Rino, "On the application of phase screen models to the interpretation of ionospheric scintillation data," *Radio Sci.*, vol. 17, no. 4, pp. 855–867, Jul. 1982.

[7] C. S. Carrano, K. M. Groves, and R. G. Caton, "Simulating the impacts of ionospheric scintillation on L band SAR image formation," *Radio Sci.*, vol. 47, no. 4, pp. 1–14, Aug. 2012.

[8] G. Gomba, M. Eineder, A. Parizzi, and R. Bamler, "High-resolution estimation of ionospheric phase screens through semi-focusing processing," in *Proc. IEEE Geosci. Remote Sens. Symp.*, Jul. 2014, pp. 17–20.

[9] J. Aarons, "Global morphology of ionospheric scintillations," *Proc. IEEE*, vol. 70, no. 4, pp. 360–378, Apr. 1982.

[10] L. Alfonsi et al., "Analysis of the regional ionosphere at low latitudes in support of the biomass ESA mission," *IEEE Trans. Geosci. Remote Sens.*, vol. 56, no. 11, pp. 6412–6424, Nov. 2018.

[11] B. H. Briggs, "Ionospheric irregularities and radio scintillations," *Contemp. Phys.*, vol. 16, no. 5, pp. 469–488, Sep. 1975.

[12] C. Rino, *The Theory of Scintillation With Applications in Remote Sensing*. Hoboken, NJ, USA: Wiley, 2011.

[13] D. L. Knepp, "Multiple phase screen calculation of two-way spherical wave propagation in the ionosphere," *Radio Sci.*, vol. 51, no. 4, pp. 259–270, Apr. 2016.

[14] M. Shimada, Y. Muraki, and Y. Otsuka, "Discovery of anoumoulous stripes over the Amazon by the PALSAR onboard ALOS satellite," in *Proc. IEEE Int. Geosci. Remote Sens. Symp.*, Jul. 2008, pp. 387–390.

[15] D. P. Belcher and P. S. Cannon, "Amplitude scintillation effects on SAR," *IET Radar, Sonar Navigat.*, vol. 8, no. 6, pp. 658–666, Jul. 2014.

[16] H. Sato, J. S. Kim, Y. Otsuka, C. M. Wrasse, E. R. de Paula, and J. R. de Souza, "L-band synthetic aperture radar observation of ionospheric density irregularities at equatorial plasma depletion region," *Geophys. Res. Lett.*, vol. 48, no. 16, p. 2021, Aug. 2021.

[17] J. S. Kim, K. P. Papathanassiou, H. Sato, and S. Quegan, "Detection and estimation of equatorial spread F scintillations using synthetic aperture radar," *IEEE Trans. Geosci. Remote Sens.*, vol. 55, no. 12, pp. 6713–6725, Dec. 2017.

[18] J. S. Kim, K. P. Papathanassiou, R. Scheiber, and S. Quegan, "Correcting distortion of polarimetric SAR data induced by ionospheric scintillation," *IEEE Trans. Geosci. Remote Sens.*, vol. 53, no. 12, pp. 6319–6335, Dec. 2015.

[19] B. Nava, P. Coïsson, and S. M. Radicella, "A new version of the NeQuick ionosphere electron density model," *J. Atmos. Sol.-Terr. Phys.*, vol. 70, no. 15, pp. 1856–1862, Dec. 2008.

[20] D. Bilitza, "IRI the international standard for the ionosphere," *Adv. Radio Sci.*, vol. 16, pp. 1–11, Sep. 2018.

[21] F. J. Meyer, K. Chotoo, S. D. Chotoo, B. D. Huxtable, and C. S. Carrano, "The influence of equatorial scintillation on L-band SAR image quality and phase," *IEEE Trans. Geosci. Remote Sens.*, vol. 54, no. 2, pp. 869–880, Feb. 2016.

[22] B. N. Anoop, P. E. Ameenudeen, and J. Joseph, "A meta-analysis of contrast measures used for the performance evaluation of histogram equalization based image enhancement techniques," in *Proc. 9th Int. Conf. Comput., Commun. Netw. Technol. (ICCCNT)*, Jul. 2018, pp. 1–6.

[23] C. V. Jakowatz, D. E. Wahl, P. H. Eichel, D. C. Ghiglia, and P. A. Thompson, "Phase errors and autofocus in SAR imagery," in *Spotlight-Mode Synthetic Aperture Radar: A Signal Processing Approach*. Boston, MA, USA: Springer, 1996, pp. 221–271.

[24] S. Ji, W. Chen, X. Ding, and C. Zhao, "Equatorial ionospheric zonal drift by monitoring local GPS reference networks," *J. Geophys. Res., Space Phys.*, vol. 116, no. A8, Aug. 2011, Art. no. A08310.

[25] P. Prats, A. Reigber, and J. J. Mallorqui, "Topography-dependent motion compensation for repeat-pass interferometric SAR systems," *IEEE Geosci. Remote Sens. Lett.*, vol. 2, no. 2, pp. 206–210, Apr. 2005.